Monthly Notices
of the
ROYAL ASTRONOMICAL SOCIETY
MNRAS **455,** 1892–1904 (2016) doi:10.1093/mnras/stv2344

Ceres water regime: surface temperature, water sublimation and transient exo(atmo)sphere

M. Formisano,[1⋆] M. C. De Sanctis,[1⋆] G. Magni,[1⋆] C. Federico[2] and M. T. Capria[1]

[1]*INAF-IAPS, Via del Fosso del Cavaliere 100, 00133 Rome, Italy*
[2]*Dipartimento di Fisica e Geologia - Universitá di Perugia, 06123 Perugia, Italy*

Accepted 2015 October 6. Received 2015 October 5; in original form 2015 July 30

ABSTRACT

Recent observations of water emission around Ceres suggest the presence of an ice layer on or beneath the surface of this asteroid. Several mechanisms have been suggested to explain these plumes, among which cometary-like sublimation seems to be plausible, since there is a correlation between the magnitude of the emission and the change in the heliocentric distance along the orbit. In this work, we applied a comet sublimation model to study the plausible scenarios that match with Herschel observations of the water flux (10^{26} molecules s^{-1}). Each scenario is characterized by a well-defined set of physical and orbital parameters. Moreover, a study of the dynamic evolution of the H_2O plume has been performed, showing that an optically thin transient atmospheric envelope, with a typical timescale of some tens of days, can be maintained by the H_2O surface emission. Our simulations could be useful theoretical support for the *Dawn* NASA mission by giving a better understanding of the physical conditions for water sublimation and ice stability.

Key words: minor planets, asteroids: individual: Ceres – planets and satellites: interiors – planets and satellites: atmospheres.

1 INTRODUCTION

Ceres is one of the two targets of the *Dawn* NASA mission (Russell & Raymond 2011). *Dawn*, after visiting Vesta in 2011, moved to Ceres to study this object, which seems to be the key for reconstructing the water history of the Solar system. With its equatorial and polar radius of 487.3 ± 1.8 km and 454.7 ± 1.6 km (Thomas et al. 2005), respectively, Ceres is the biggest object of the main asteroid belt. It is also the most massive body, since it contains about a third of the overall mass of the belt (Carry et al. 2008). Ceres is thought to be differentiated into a silicate core (with, probably, a weak presence of metals), and an icy mantle (A'Hearn & Feldman 1992; McCord & Sotin 2005; Castillo-Rogez & McCord 2010), while hydrated minerals have been found on its surface (McCord, Castillo-Rogez & Rivkin 2011). Its low density, 2.077 ± 0.036 g cm^{-3} (Thomas et al. 2005), suggests a high content of ice up to 30 per cent wt, if its porosity is low. Moreover, water emission from Ceres has been recently reported by Küppers et al. (2014) from Herschel observations. Water emission was also suggested due to the marginal detection of the photo-dissociation product OH (A'Hearn & Feldman 1992). Küppers et al. (2014) showed that the detected water vapour around Ceres (at least 10^{26} molecules s^{-1}) probably originates from localized sources at mid-latitude regions on the surface. Since such observations appear to be dependent on heliocentric distance, with the peak of activity concentrated at perihelion passage, the origin of this vapour could be due to comet-like sublimation. However, we need more data to constrain the mechanism of this activity because we do not a priori exclude other mechanisms such as cryo-volcanism. This latter mechanism requires an interior source of energy, which could be the dissipation of tidal forces (as happens for ice satellites, i.e., Io and Enceladus) or due to long-lived radionuclides. As we can reasonably neglect dissipation by tidal forces for Ceres, we want to point out that some models (McCord et al. 2011, and references therein) propose long-lived radioisotopes as possible candidates to feed cryo-volcanism. More recently, Shoji & Kurita (2014) suggested that compositional diapirism could represent a way to carry buried ice towards the surface and to explain water flux emission.

In the literature, there are several publications on the thermal evolution of Ceres (McCord & Sotin 2005; Castillo-Rogez & McCord 2010), but they simulate the thermal interior evolution (and consequently the onset of the chemical/physical differentiation) since its formation from the solar nebula. Ceres's water flow regime was also simulated by Fanale & Salvail (1989). They investigated the conditions for ice stability beneath the surface by applying a thermophysical model in one dimension. Their simulations suggest stable ice, which survives for 4.5 billion years, at a depth of 10–100 m at the equator and at a depth less than 10 m at latitudes greater than

⋆ E-mail: michelangelo.formisano@iaps.inaf.it (MF); mariacristina.desanctis@iaps.inaf.it (MCD); gianfranco.magni@iaps.inaf.it (MG)

© 2015 The Authors
Published by Oxford University Press on behalf of the Royal Astronomical Society

Downloaded from https://academic.oup.com/mnras/article-abstract/455/2/1892/1108445 by guest on 07 May 2020

40°. Moreover, they found that ice on the surface with an albedo of 0.1 (the same as Ceres as a whole) could not survive for latitudes less than or equal to 80°.

A recent study (Tu, Ip & Wang 2014) analyses different physical mechanisms as possible drivers for an exosphere in Ceres. Sublimation (with a production rate of 10^{24} molecules s^{-1}) of buried ice in subsurface layers or localized emission of gas plumes (or, ultimately, a combination of both mechanisms) could explain the development of an exosphere of global scale. The authors found that the dynamic lifetime of this exosphere (considering two rates of water production, 10^{24} molecules s^{-1} and 10^{25} molecules s^{-1}) is about 10^5 s.

Water emission from Ceres is not constant along the orbit (Küppers et al. 2014), suggesting sublimation driven by the change in heliocentric distance along the orbit. For this reason, here, we applied the cometary-like model described in Lasue et al. (2008) and De Sanctis et al. (2010a,b), derived from the thermal evolution of cometary nuclei, which uses a quasi-3D approach to study the thermal properties of the surface and the possible water activity. The model uses a shell structure and, since we are not interested in the overall internal thermal history but rather the surface and subsurface layers, we can reasonably apply this model to an object, i.e., Ceres, larger than a comet. In this work, we want to investigate the likely scenarios that fit with Herschel observations of the water flux (10^{26} molecules s^{-1}). We evaluated how physical (albedo, dust/ice ratio, thermal conductivity and ice depth) and orbital parameters could affect sublimation and surface/subsurface temperature, and if the ice is stable on the surface or not. We also provided an estimation of the area required for emitting to reproduce the water flux observed by Herschel. In the following, we briefly describe the key points of our model and we refer the reader to Lasue et al. (2008) and De Sanctis et al. (2010a,b) for more exhaustive details.

Moreover, a numerical model of the dynamic evolution of dust and H_2O vapour (Magni 2014; Magni G., in preparation), based on smoothed-particle hydrodynamics (SPH) and Monte Carlo techniques, was also utilized to study the behaviour and the main physical parameters of the matter emitted by the surface of Ceres over a typical time interval of several days.

2 THE MODEL

The model assumes Ceres to be a spherical body with initial radius of 469 km. Since we are interested only in the water emission and surface/subsurface temperature, we model the subsurface layer down to a depth of 100 m only. A spatial grid of 0.005 m is used. The model is labelled quasi-3D because the illumination for each of the facets, covering the entire surface of the asteroid, is calculated by the angle between the local normal and the direction of the Sun. The code solves the following heat diffusion equation:

$$\rho c \frac{\partial T}{\partial t} = \nabla \cdot [k \nabla T] + Q_{H_2O}, \quad (1)$$

where ρ is the density, c is the specific heat of the asteroid material, k is the thermal conductivity and Q_{H_2O} is the specific energy gained or lost by the solid matrix due to sublimation and re-condensation of the water ice. The mass conservation equation controls the gas flow through the pore system:

$$\frac{\partial \rho_g}{\partial t} = -\nabla \Phi + Q^*, \quad (2)$$

where ρ_g is the density of the gas, Φ is the gas flux and Q^* is the gas source term due to both sublimation and re-condensation. We assume that the ideal gas regime is valid.

Table 1. Main fixed physical and orbital parameters used in this work.

Parameters	Value	Units
Radius (R_{Ceres})	469	[km]
Rotational period (T_{rot})	9.074	[h]
Orbital period (T_{orb})	4.60	[yr]
Large semi-major axis (ax)	2.765	[au]
Eccentricity (e)	0.079	
Mean pore radius (r_g)	1×10^{-4}	[m]
Ice depth	[100,0.5,0.05,0.02,0]	[m]
Emissivity (e)	0.8	

Table 2. Summary of scenarios we developed. Only for scenarios M0–M3 did we investigate several values of ice depth (see Table 1). For M4 and M5, we investigated only the case of exposed ice. d/i is the dust/ice ratio, k_{cr} is the thermal conductivity of the crust (W m^{-1} K^{-1}), T_{in} is the initial temperature (K), I is the thermal inertia (J m^2 K^{-1} $s^{-1/2}$), a is the albedo and ϕ is the latitude.

Scenario	(d/i)	k_{cr}	T_{in}	I	a	ϕ
M0	2.5	10^{-3}	163	≃40	0.09	0°
M1	2.5	10^{-3}	163	≃40	0.09	45°
M2	2.5	10^{-3}	163	≃40	0.09	80°
M3	2.5	10^{-2}	163	≃130	0.09	0°
M4	0.5	3	100	≃2000	0.5	0°
M5	0.1	3	100	≃2000	0.9	0°

2.1 Boundary conditions

The surface temperature is derived from the balance among solar input and energy re-emitted to space, conducted to the interior or used to sublimate ice:

$$\frac{S(1-A)\cos Z}{R_h^2} = \varepsilon \sigma T_s^4 + k(T_S) \left.\frac{dT}{dz}\right|_{sup} + f H(T_S) v(T_S),$$

where S represents the solar constant, R_h is the heliocentric distance of Ceres, A is the Bond albedo, Z is the local zenith angle, ε is the emissivity of the surface, σ is the Stefan–Boltzmann constant, f is the surface fraction covered by water ice, H is the latent heat of sublimation and v is the sublimation rate. The temperature boundary condition at the centre, i.e., at a depth of 100 m is:

$$\frac{\partial T}{\partial z} = 0. \quad (3)$$

2.2 Physical and orbital parameters and scenarios developed

In Table 1, we report the main physical parameters of our model. The orbit of Ceres is nearby circular (0.079) with a mean heliocentric distance of 2.77 au and a spin axis obliquity of 9°(data provided from JPL Small-Body Database Browser). The rotational period is about 9 h (Chamberlain, Sykes & Esquerdo 2007), while the orbital period is 4.60 yr. In this paper, we performed several simulations to study the effects of the different parameters on temperature and on sublimation. The emissivity is set to 0.8 to simulate a moderately rougher surface. Silicate dust and ice are in well-defined proportions and homogeneously distributed in the overall structure. The initial pore radius is set to 10^{-4} m (Capria et al. 2012).

We developed six scenarios (labelled M0–M5, see Table 2), characterized by different dust/ice ratios, thermal conductivities and albedoes, and we explored three latitudes: the equator, 45° and 80°. For the M0, M1, M2 and M3 scenarios, the ice front is set at different depths from the surface, in some cases compatible with the

Downloaded from https://academic.oup.com/mnras/article-abstract/455/2/1892/1108445 by guest on 07 May 2020

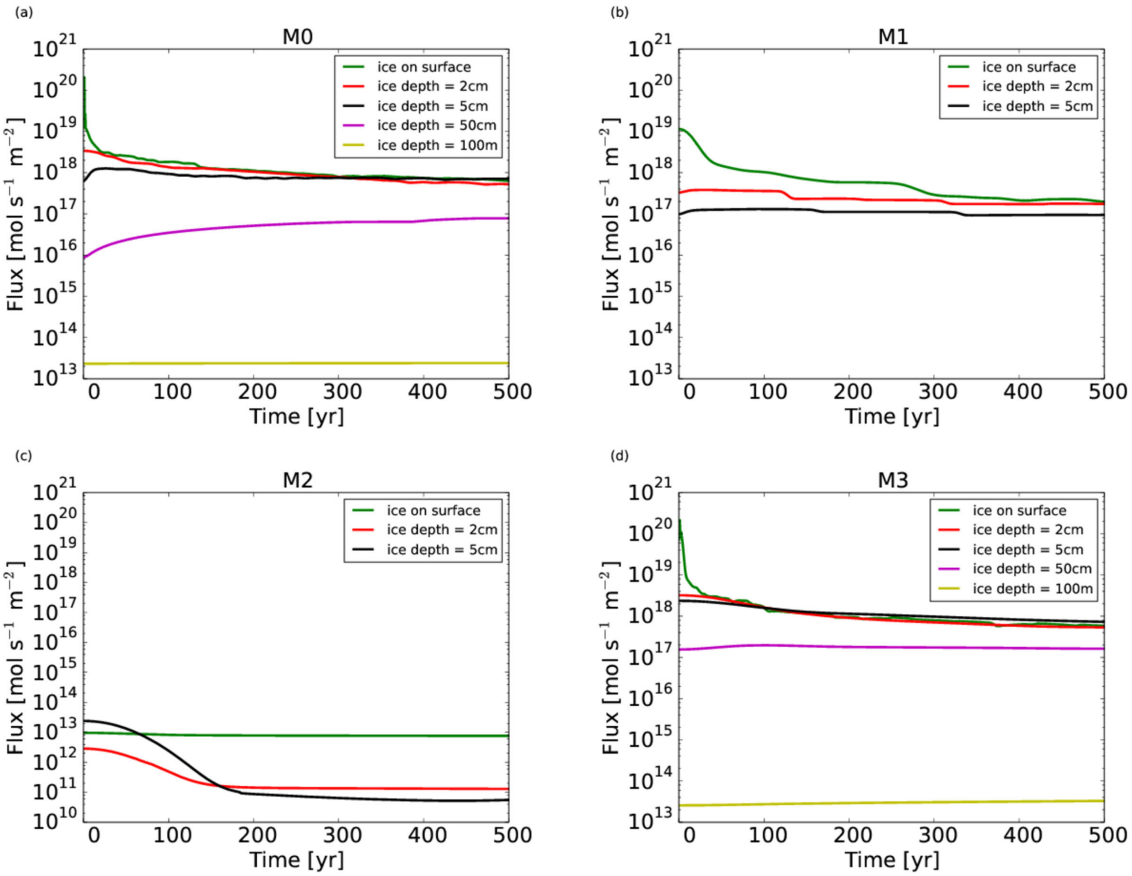

Figure 1. Flux of water versus time for M0 (a), M1 (b), M2 (c) and M3 (d), for different ice depths. For the mid-latitude ($\phi = 45°$) and near the pole ($\phi = 80°$), we explored only ice depths compatible with the annual skin depth.

diurnal skin depth (a few centimetres) while in others well below the skin depth (both diurnal and orbital). Recall that the thermal skin depth give us an idea of how the thermal wave penetrates the surface. Quantitatively, it is the distance at which the wave is attenuated by a factor $1/e$. The initial temperature is fixed at 163 K, i.e., the temperature for a surface in radiative equilibrium at Ceres's mean orbital radius, by assuming a solar constant of 1370 W m^{-2}. This parameter is crucial for the thermal evolution of the asteroid and in particular, for sublimation of water ice. We want to point out that for buried ice, the dust/ice ratio of the first layers, hereafter the crust, is not the same as in the remaining layers, because ice is not present in the crust. This crust is made of only porous silicate dust, whose thermal conductivity (for the several scenarios) is shown in Table 2. All the other layers have the initially fixed dust/ice ratio. During the thermal evolution, the crust grows as long as the ice recedes.

We explored several values of the thermal conductivity of the crust (k_{cr}) to evaluate how the thermal wave penetrates into the subsurface layers and consequently how surface temperature and sublimation rates are affected. For a dust/ice ratio of 2.5, the values used are 10^{-3} and 10^{-2} W m^{-2} K^{-1} (henceforward [SI]). These values are in agreement with the experiments of Krause et al. (2011) on porous dust samples. We also developed two cases, nearly pure ice (M4) and pure ice (M5), characterized by dust/ice ratios of 0.5 and 0.1, respectively. The thermal conductivity is set to 3 [SI] (according to the temperature dependence studied in Klinger 1980) and the albedo is fixed at 0.5 (M4) and 0.9 (M5). In M4 and M5, we analysed only the case of ice on the surface and equatorial latitude, while in the other scenarios (M0–M3) also the effect of latitude on water flux and temperature is investigated. In these cases, the initial temperature is set to a lower value than in the first cases, i.e., 100 K.

3 RESULTS

By starting from a case study, i.e., the M0 scenario, we explored how physical (albedo, dust/ice ratio and thermal conductivity) and orbital (latitude) parameters could affect temperature and the water emission rate. In the following sections, we examine the different cases we explored. The results can be seen in Figs 1–8.

3.1 High dust/ice ratio cases: M0–M3

We assume that the spherical Ceres is a fast rotator (i.e., diurnal variations are neglected). The simulation time covered is 500 yr. From our simulations (see Fig. 1a), it is clear that the ice on the surface and at the equatorial latitude is very unstable (it lasts for only a very few orbits, more or less 10 yr). The water flux reaches its maximum at 10^{21} mol s^{-1} m^{2} (henceforward [SI]) before stabilizing at a value near 10^{18} [SI]. Ice covered by a thin silicate dust blanket is more stable for many orbits, and also in this case the value is around 10^{18} [SI]. If the ice is buried beneath the surface, the water flux is very low. It is 10^{16} [SI] if the icy front is 50 cm from the surface and 10^{13} [SI] if 100 m. Neglecting the case in which the ice is very buried, we analyse how the latitude influences the emission. For the mid-latitude (Fig. 1b), there are no large differences from the equatorial case, while near the pole (see Fig. 1c), due to the

Downloaded from https://academic.oup.com/mnras/article-abstract/455/2/1892/1108445 by guest on 07 May 2020

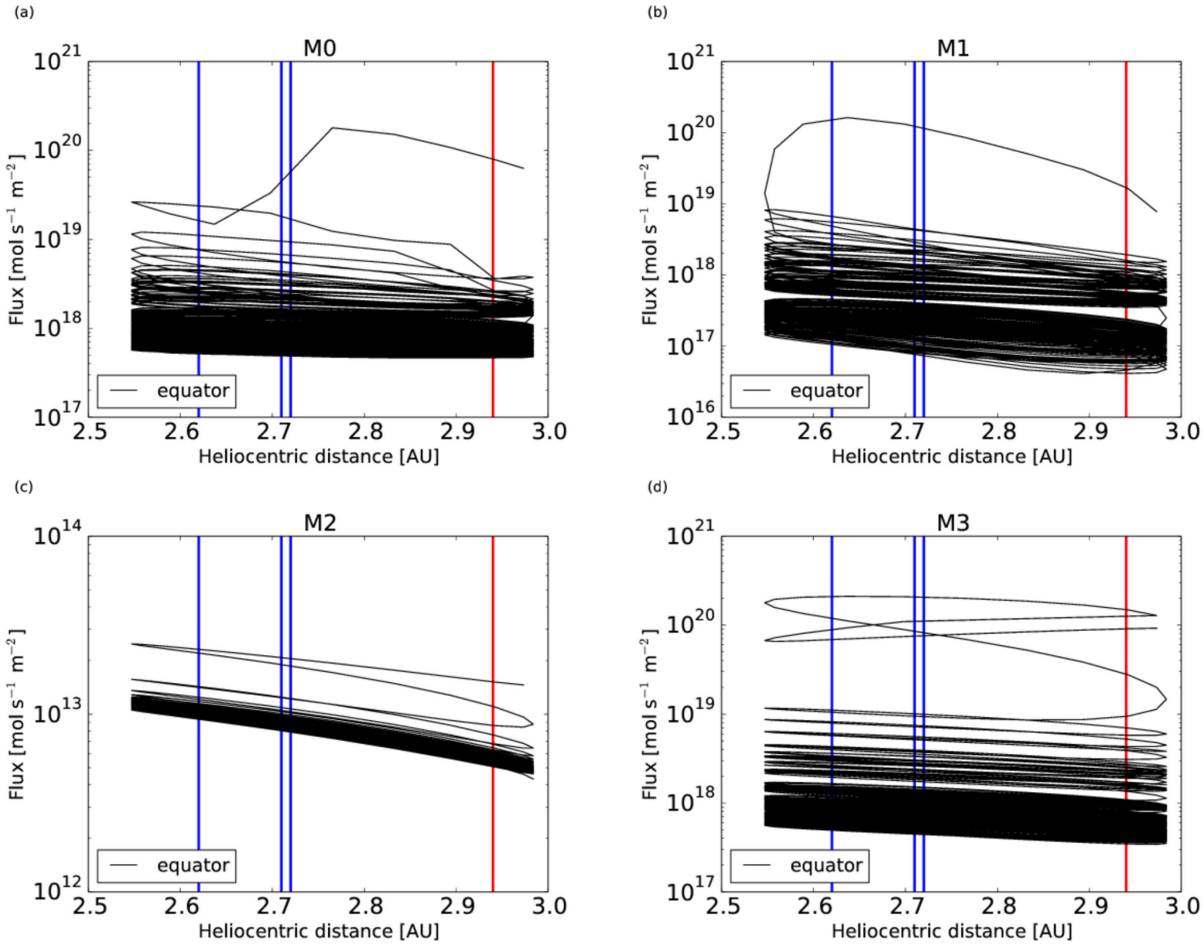

Figure 2. Flux of water versus heliocentric distance for M0 (a), M1 (b), M2 (c) and M3 (d), for ice on the surface at the equatorial latitude. Vertical blue lines correspond to the heliocentric distance of water line detections, and the red line to no detection (Küppers et al. 2014).

low illumination conditions, we notice that the ice is very stable and consequently the water emission is very low. On increasing the crust thermal conductivity (M3), we observe only a weak increase in the emission even if the general trend is similar to M0. For $d/i = 2.5$ and $k_{cr} = 10^{-3}$ [SI] (M0–M2), the thermal inertia (I) is about 40 [SI], by assuming a specific heat of 800 [SI]. For $k_{cr} = 10^{-2}$ [SI], I is more than 100 [SI]. The thermal inertia gives us an idea of how a body reacts to a change of temperature and so gives an indication of the material constituting the body. It is expected that Ceres could have low/medium values of thermal inertia. Some studies suggest values of 15–38 [SI] (Spencer 1990; Chamberlain, Lovell & Sykes 2009), others higher values, i.e., 80 (Keihm et al. 2013).

Fig. 2 shows the water flux emission along the orbit for all scenarios we developed. Blue lines correspond to the heliocentric distances (2.62, 2.65, 2.71 and 2.72 au) where water emission was detected while it was not observed at 2.94 au (red line). In all the plots of Fig. 2, the transition phase during which ice on the surface starts to recede is evident. At the poorly illuminated pole (M2), this phase is less appreciable.

In Fig. 3, we report the temperature profile versus heliocentric distance. The range of values reached in M0, M1 and M3 is the same [≅175, ≅190 K]. Thermal conductivity does not significantly change the surface temperature (see Figs 3a and c). As well, at the mid-latitude, we have the same values (Fig. 3b). At the pole (Fig. 3c), the temperature ranges from about 115 K to about 125 K.

3.1.1 Day–night profile

In Fig. 4, we show a day–night surface temperature profile for M0–M3 at the heliocentric distance of the first detection of water emission (2.72 au). Obviously, in this case, we do not assume that Ceres is a fast rotator. We report only the cases of exposed ice (Fig. 4a) and 2 cm beneath the surface (Fig. 4b), since for ice further below the surface, the temperature profile is quite similar to the 2-cm case. For exposed ice (Fig. 4a), the temperature is lower due to the large albedo. The maximum temperature is reached in M0 (at the equator) around 190 K. We do not notice large temperature variations due to the thermostatic effect of the ice transition phase. In Fig. 4(b), high temperatures are reached during the day (for example, in M0, close to the blackbody temperature). For the M0 case (low thermal conductivity and at the equator), the maximum surface temperature achieved is consistent with Visible and Infrared Spectrometer (VIR) measurements (Tosi et al. 2015) and with the temperature of the warmest area (235 ± 4 K) (Saint-Pe, Combes & Rigaut 1993). During the night, due to the low thermal conductivity, the thermal wave penetrates poorly inside the body. The consequence is that the night temperatures in Fig. 4(b) are lower than the corresponding ones of Fig. 4(a).

In general, a high albedo (exposed ice) influences the maximum temperatures through the thermostatic effect of the ice transition phase, while thermal conductivity influences the temperature variations.

Downloaded from https://academic.oup.com/mnras/article-abstract/455/2/1892/1108445 by guest on 07 May 2020

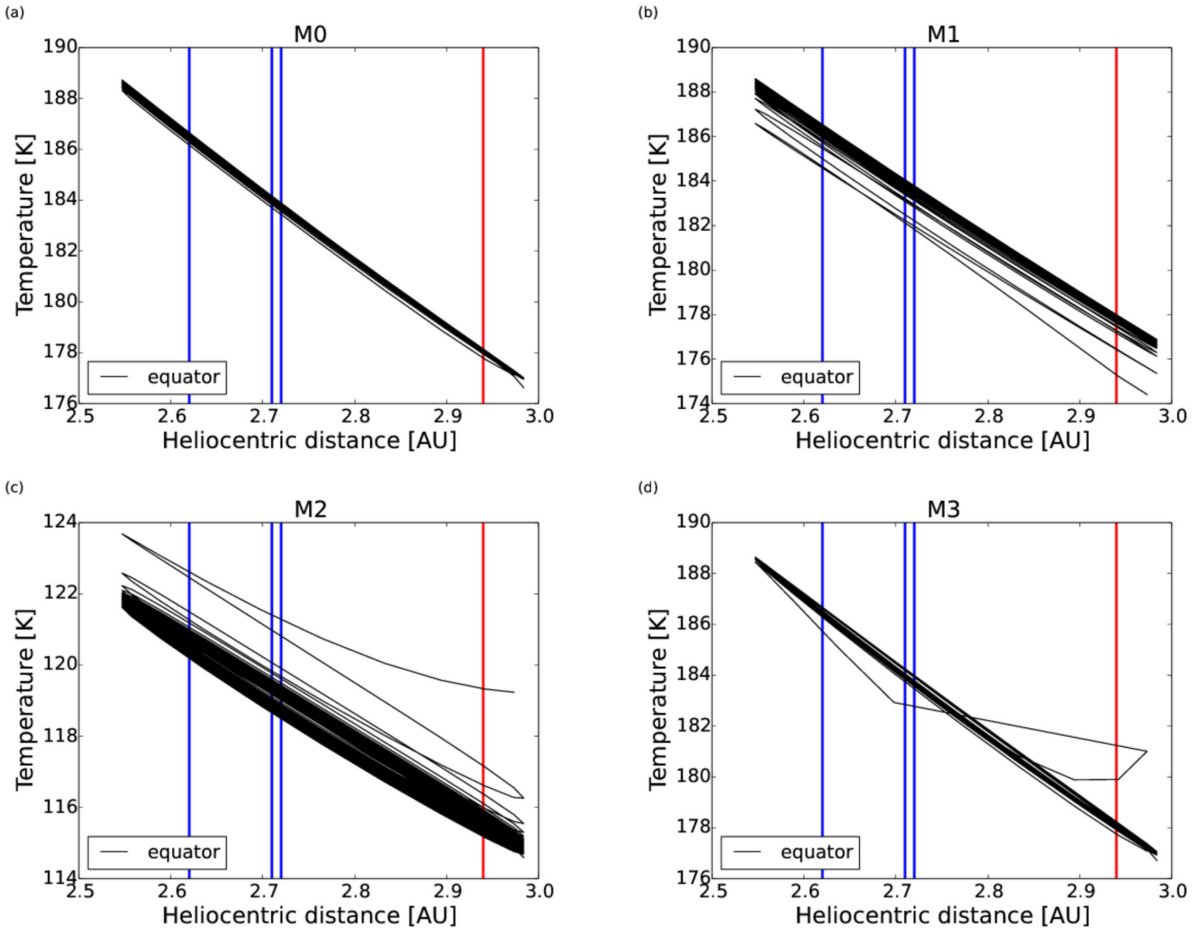

Figure 3. Surface temperature versus heliocentric distance for M0 (a), M1 (b), M2 (c) and M3 (d), for ice on the surface at the equatorial latitude. Vertical blue lines correspond to the heliocentric distance of water line detections, and the red line to no detection (Küppers et al. 2014).

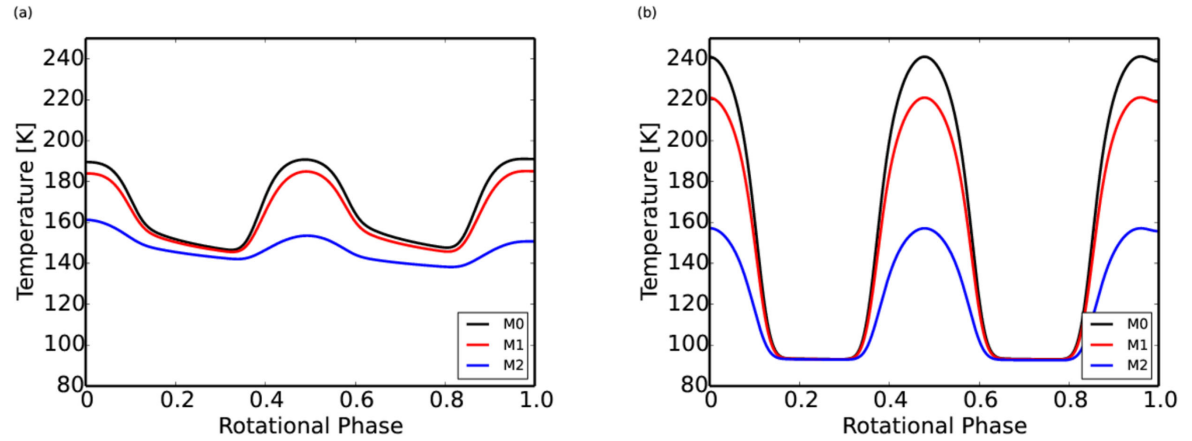

Figure 4. Daily temperature cycle for M0–M2 with ice on surface (a) and buried 2 cm beneath the surface (b).

3.1.2 Stratigraphy

The stratigraphy of Fig. 5 (only for ice on the surface and buried 2 and 5 cm beneath the surface, for M0–M3) shows the evolution of the ice front during the time of simulation (500 yr). In Fig. 5(a), we observe that in all cases (exposed or buried ice), the icy front reached more or less the same values (15 cm) after 500 yr. In Fig. 5(b), there are ice depth changes of a few centimetres. In Fig. 5(c), the profile is flat (no change in icy front depth). In Fig. 5(d), the ice reaches, in all cases, a depth of about 20 cm. The different stratigraphies among the different cases simply reflect the different production rates.

3.1.3 Dependence on emissivity

We noticed that a change in emissivity when considering a smooth surface ($e = 0.9$) led to very similar results for both water emission and temperature, as we can see in Fig. 6. The maximum and

Downloaded from https://academic.oup.com/mnras/article-abstract/455/2/1892/1108445 by guest on 07 May 2020

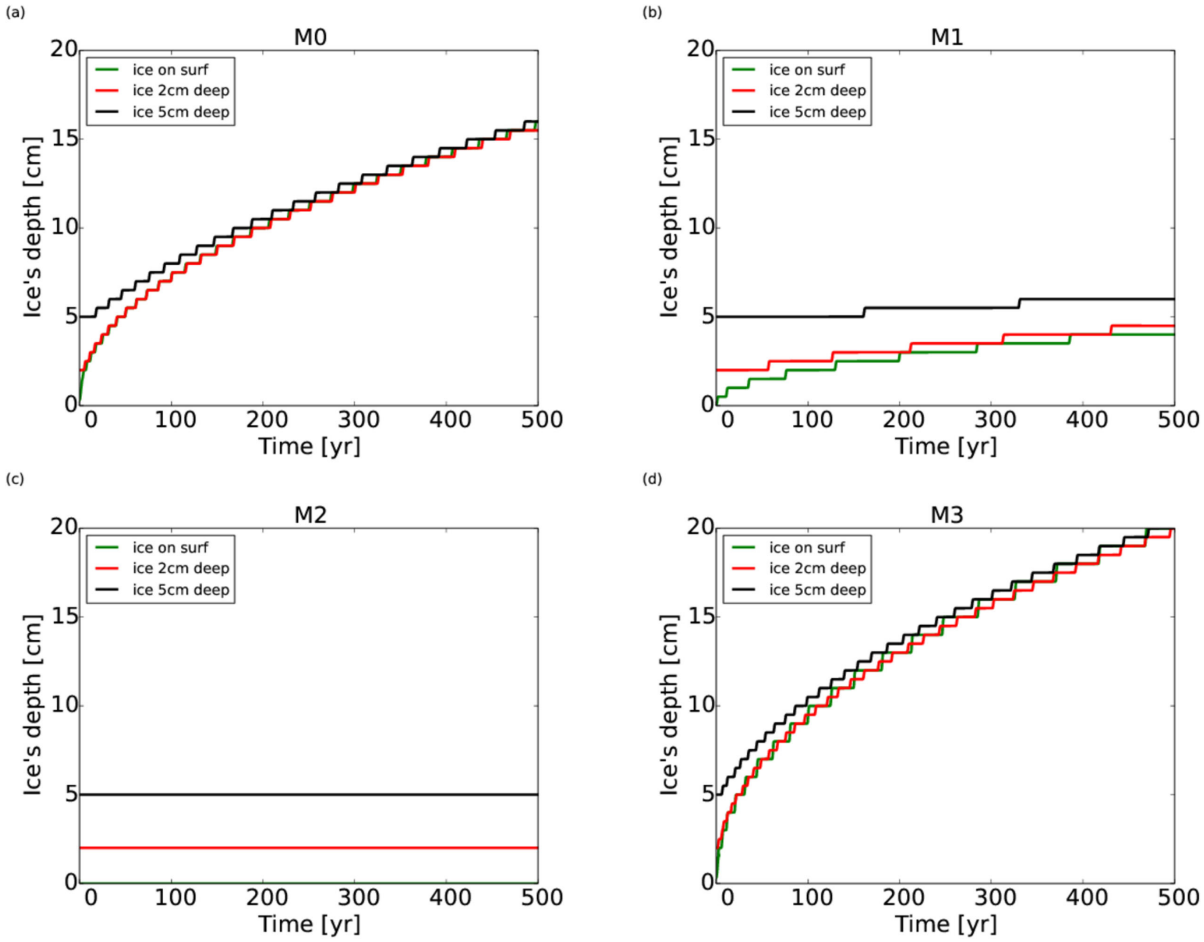

Figure 5. Ice front depth as a function of time for for M0 (a), M1 (b), M2 (c) and M3 (d). We neglect cases in which the ice is very buried beneath the surface.

minimum values reached are more or less the same in both cases, but for the general trend, we notice a broader behaviour for an emissivity of 0.9.

3.1.4 Internal temperature

Fig. 7 reports the temperature profile versus time. We focus on the last simulated orbits. We show only the case M0 with ice initially on the surface. Different depths are explored (compatible with the annual skin depth), to evaluate the decrease of temperature in the subsurface layers. The maximum temperature changes from 190 K on surface to about 175 K at 50 cm deep. Ceres is assumed to be a fast rotator.

3.2 Nearly pure (M4) and pure ice (M5) cases

Fig. 8 shows the cases for nearly pure ice (M4) and pure ice (M5). The water flux emission profile (mediate on overall orbit) is shown in Fig. 8(a). In M4, the values are stable around 10^{18} [SI], while in M5 they are very low (10^{10} [SI]). The stratigraphy shows how the ice in the M4 case moved from the surface to a depth of 1 m (Fig. 8b). Figs 8(c) and (d) depict the water flux emission along the orbit for M4 and M5, respectively. Values range from 10^{17} [SI] up to 10^{19} [SI] for M4 and they are very low for M5 (between 10^{10} and 10^{11} [SI]). Until the ice is exposed on the surface, the surface temperature is around 155 K. As soon as the ice begins to recede, the temperature increases up to 185 K. In M5, it is quite constant around 105 K. The high thermal conductivity (3 [SI]) leads to a very high thermal inertia (more than 1000 [SI]).

3.3 H_2O emission and transient atmosphere

A numerical model of the dynamic evolution of the H_2O vapour emitted by bodies of asteroidal size and larger has been developed (Magni 2014), joining the treatment of the gas pressure with a SPH algorithm (Monaghan 1992, 2005), a Monte Carlo approach to the thermal escape of single molecules, and introducing thermal and dynamic effects of the dust on the evolution of H_2O vapour around Ceres.

There are several reasons why the dynamics of cold gas from volatile species (H_2O, CO_2, CH_4 and others), emitted by dwarf planets like Ceres, requires a rather different and refined treatment with respect to that for smaller-mass asteroids, where the molecules leave the surface with velocities very close to the thermal velocity:

(i) Ceres has a thermal mean velocity and surface gravitational escape velocity comparable in magnitude ($v_{\rm esc} = 500$ m s^{-1} at the surface, $v_{\rm therm} = 300$–500 m s^{-1}, depending on latitude and on local time).

(ii) Temperature variations can be large enough to allow both condensation and evaporation of H_2O, creating cold traps and ice reservoirs in the nocturnal phase and/or in polar regions, enlarging the survival cycle of the H_2O vapour.

Downloaded from https://academic.oup.com/mnras/article-abstract/455/2/1892/1108445 by guest on 07 May 2020

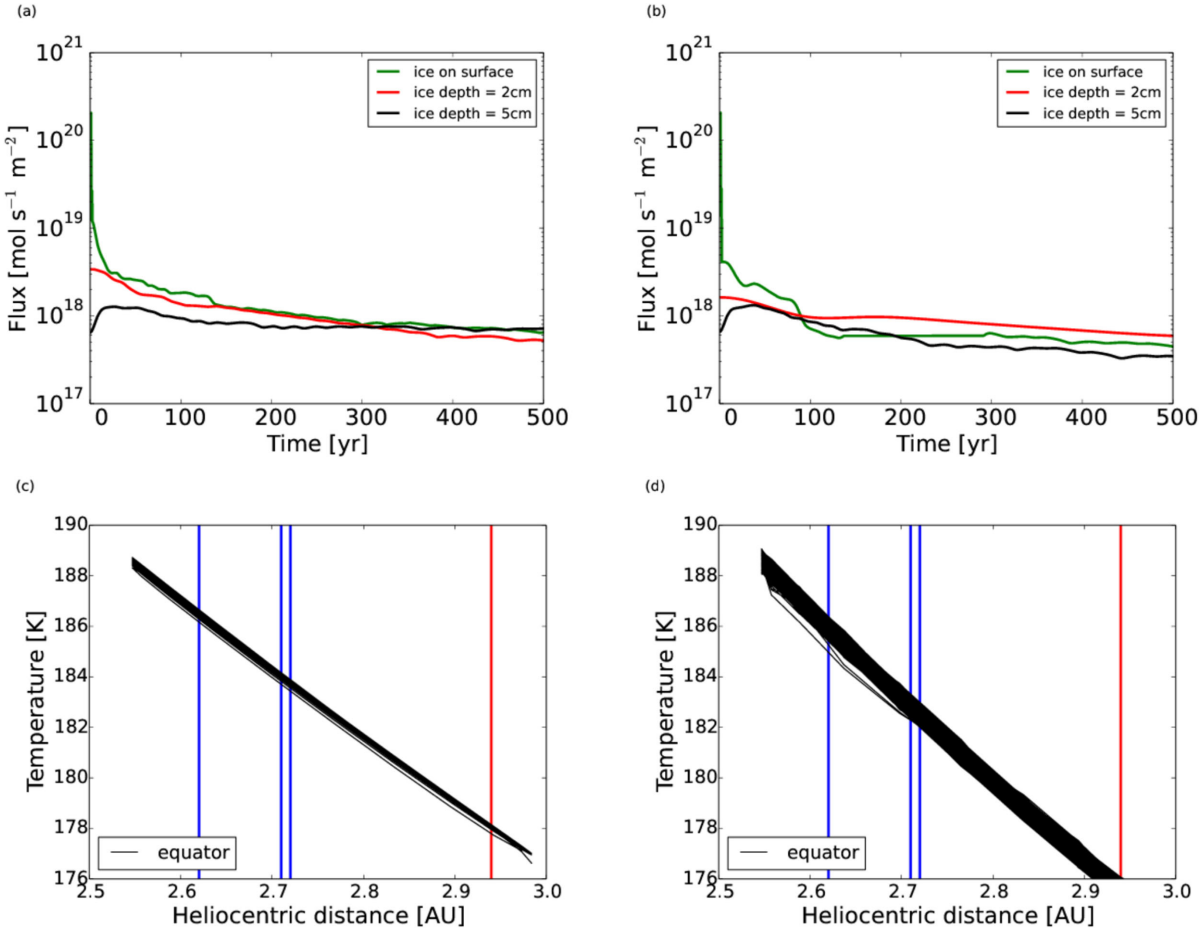

Figure 6. Comparison of flux for emissivities of 0.8 (a) and 0.9 (b) and, analogously, of surface temperature (c) and (d). In the plots for flux emission, we considered only an ice depth compatible with the annual skin depth (or not very large).

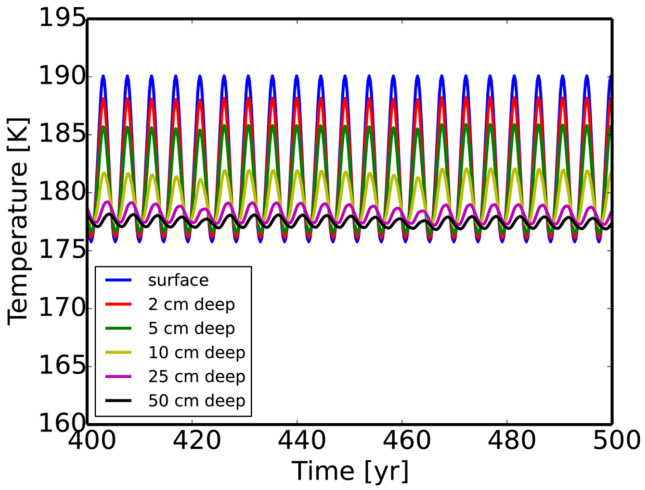

Figure 7. Internal temperature for the M0 case with ice on the surface, for different depths from the surface.

(iii) The presence of an extended Hill lobe (>2 × 10^5 km), where the planet's gravity is active, favours the accumulation of gas, which, if the emission from the surface is large enough, can produce an isothermal optically thin local thermodynamic equilibrium (LTE) envelope, whose equilibrium is driven by collisional processes. So, together with the classical thermal escape (Hunten 1973), an outward hydrodynamic flux is also present.

(iv) The dusty component, and first of all the smallest particles, due to viscous coupling, can damp the gas motion. The dust particles feel the gravity but are not subjected to pressure forces. Dust can subtract momentum from the gas, and at the same time, due to its high opacity, it cools the gas and lowers its mean thermal velocity. Finally, the dust, when the density is low enough, decouples itself from the gas, and a fraction of it can ultimately remain in gravitationally bound long-time orbits, accumulating and enhancing the effects on the gas.

3.3.1 Numerical treatment

The SPH formalism was adopted here because it is probably the best approach for a physical situation like a plume emission, with strong variations, in time and in space, of the density and of the main dynamic and thermodynamic parameters. The H_2O vapour is initially emitted (6 kg s^{-1}) with pressures of a few microbars and on scales of hundredths of metres, dispersing in a few days over the entire Hill lobe and reaching densities so low that the molecule mean free path is comparable with the same Hill lobe. Moreover, the typical velocities run from a fraction of the mean thermal velocity up to highly supersonic values. Finally, the temperatures can vary from the blackbody equilibrium value at Ceres's distance, to those of ice condensation.

Downloaded from https://academic.oup.com/mnras/article-abstract/455/2/1892/1108445 by guest on 07 May 2020

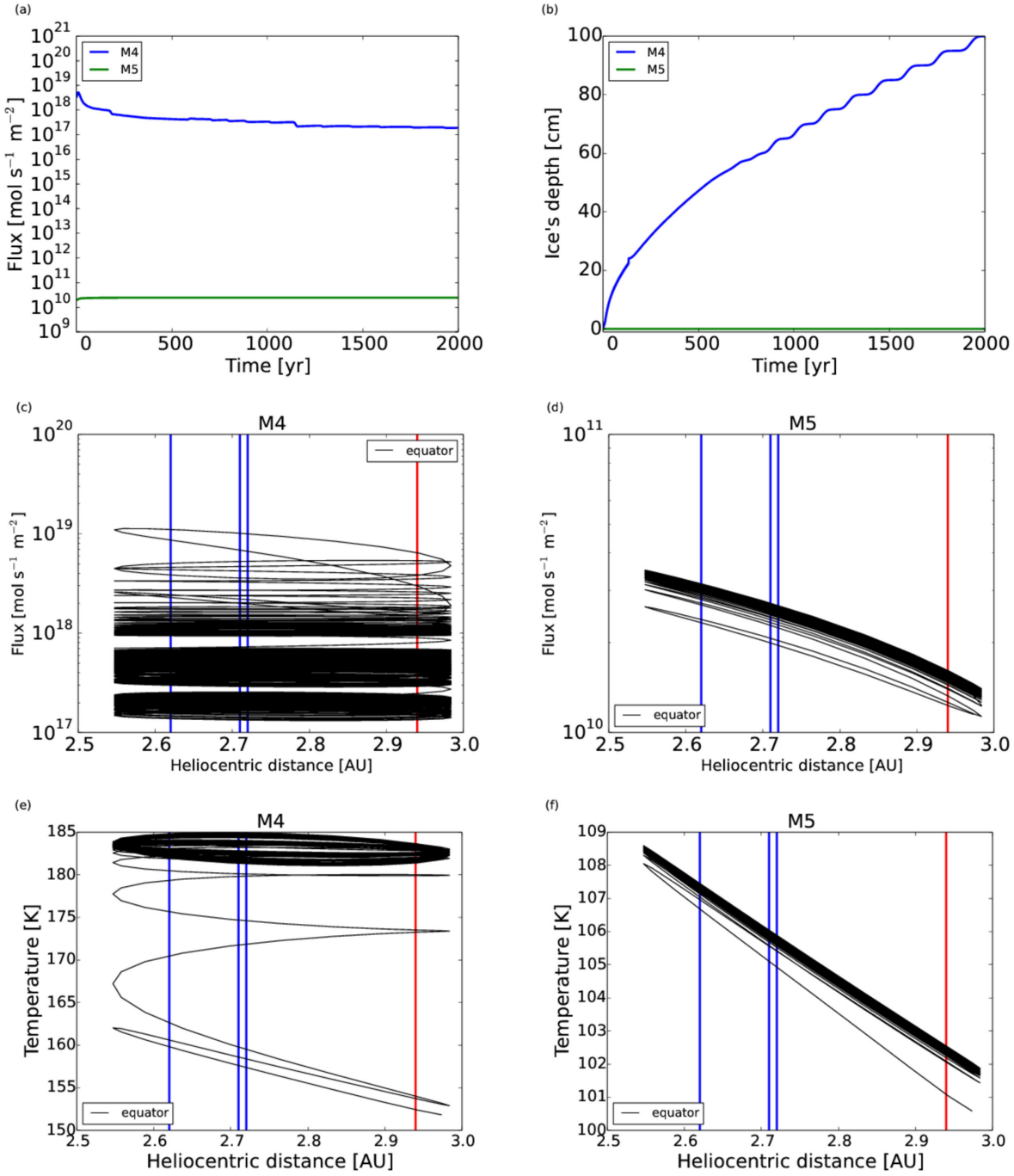

Figure 8. Flux of water (a) and ice front depth (b) versus time, for M4 and M5. (c) Flux of water versus heliocentric distance for M4 at the equator and for M5 (d). Surface temperature versus heliocentric distance at the equator for M4 (e) and for M5 (f). Vertical blue lines correspond to the heliocentric distance of water line detections, while the red line is for no detection (Küppers et al. 2014).

The SPH code was built following the basic treatment of Monaghan (1992). The gas, with total mass M_g, is divided into N pseudo-particles, with mass $m_g = M_g/N$ and each being spread in space with a suitable normalized function $W(\boldsymbol{r} - \boldsymbol{r}_b, h_b)$, the interpolating kernel. Here $\boldsymbol{r}$ is the current coordinate vector, $\boldsymbol{r}_b$ that of particle b, and h_b a local parameter that controls the spreading of the function W. The central statement of the SPH method is that any function $A(r)$, representing a dynamic or thermodynamic parameter, or its space and time derivatives (gradient, Laplacian and so on), can be approximated by an analytical sum of terms involving the parameters and the kernels, together with their first- or higher-order derivatives, computed for the positions b of the pseudo-particles (Monaghan 1992):

$$A_s(\boldsymbol{r}) = \sum_b m_b \frac{A_b}{\rho_b} W(\boldsymbol{r} - \boldsymbol{r}_b, h_b), \tag{4}$$

while the gradient is

$$\nabla A_s(\boldsymbol{r}) = \sum_b m_b \frac{A_b}{\rho_b} \nabla W(\boldsymbol{r} - \boldsymbol{r}_b, h_b). \tag{5}$$

Downloaded from https://academic.oup.com/mnras/article-abstract/455/2/1892/1108445 by guest on 07 May 2020

If A is the gas density, we have

$$\rho(\boldsymbol{r}) = \sum_b m_b W(\boldsymbol{r} - \boldsymbol{r}_b, h_b). \quad (6)$$

So, $W(\boldsymbol{r} - \boldsymbol{r}_b)$ can be interpreted as the density distribution of every particle b, and the local gas density is computed from the distribution function of the whole ensemble of particles. To save computer time, the sum necessarily has to be limited to a fraction of the particle ensemble. Besides, the accuracy of the evaluation of every physical quantity depends also on the parameters h_b, which control the degree of superposition of the kernels, and on the normalization of the kernels, which must represent the single pseudo-particles.

Last but not least, the functional form of the kernel W has to be selected among a large variety of different models (Monaghan 1992, 2005; Liu & Liu 2010). We have chosen for W the expression (Liu & Liu 2010):

$$W = \begin{cases} \frac{5\pi}{16h^3}\left(3 + 3q - \frac{3}{4}q^2\right) & \text{if } q < 2, \\ 0 & \text{if } q > 2, \end{cases}$$

with $q = |\boldsymbol{r}/h|$, which guarantees kernel normalization. The parameter h_b has been computed, for the particle b, as $h_b = f_\mathrm{h}(m_\mathrm{g}/\rho_b)^{1/3}$, f_h being an adjustable parameter of the order of 2. So, h_b is comparable with the main distance among the pseudo-particles. This choice ensures superposition of every kernel with a sufficient number of kernels of surrounding particles. The particles contributing to the sum of equation (4) are all those contained in a sphere of influence, around the particle a, with radius $R_\mathrm{s} = f_\mathrm{s} h_a$ (radius of influence).

The time evolution of the gas was followed by integrating the equations of motion and the thermal energy equation in the standard form given by Monaghan (1992). Also, the treatment of shocks follows Monaghan's approach. This formalism ensures rigorous linear and angular momentum conservation, but not conservation of total energy. The amount of adiabatic energy variation, in our computations (typical number of pseudo-particles $N = 30\,000$), is maintained under 5 per cent, while gas heating due to solar radiation produces growth of both kinetic and thermal energy.

Because of the large variations in density and temperature, and consequently in optical depth and in radiative diffusivity timescale, radiative processes can become important or dominant, especially in the limit of low densities. Here we adopted a first-order correction of thermal energy due to radiative transfer (Magni & Coradini 2004) that is completely correct in the limit of low and high densities. Two different temperature variations, radiative and adiabatic, are evaluated at each time step. They are merged with different weights, the reciprocals of adiabatic and radiative diffusion timescales respectively. In this way, the faster of the two processes prevails.

Even if the standard structure of the equations of Monaghan (1992) was utilized, a specific treatment of several aspects of the physical model was performed, to describe better the time evolution of the physical model itself.

3.3.2 *Correction of kernel parameters*

At any time step, two conditions must be verified by a suitable adjustment of the parameters f_h and f_s:

(i) The total number of particles inside the sphere of radius R_s has to be limited from 60 to 100, for a sufficiently accurate evaluation of the physical quantities and their derivatives. This is obtained by tuning the parameter f_s.

(ii) A mass normalization criterion can be added:

$$\rho_a = \sum_b \frac{m_b}{\pi R_\mathrm{s}^3}. \quad (7)$$

Here the bulk density, defined as the mass per unit volume of the particles inside the sphere of influence, must be equal to the SPH density (ρ_a). The local parameter f_h is tuned (increased or lowered) until equation (7) is verified.

3.3.3 *Boundary conditions*

A physically consistent treatment of the boundary conditions is one of the critical points in SPH modelling. In particular, when a pseudo-particle comes near a solid region (Ceres's surface), the sphere of influence of radius R_s is cut, so the computation of density and pressure is no longer consistent and the value of the pressure gradient vector is wrong. Here we have adopted that the portion of the sphere of interaction going beneath Ceres's surface is filled by mirror pseudo-particles (Monaghan 1994; Liu & Liu 2010), each one having a mass much larger than the gas ones. The mirroring is done with respect to the plane tangent to Ceres's surface, and by using the same particles that are in the free space, with symmetric space coordinates and quiescent. In this way, the pressure gradients have the right orientation. The value of the fictitious mass of the mirror particles was optimized to avoid, as much as possible, particles crossing the surface, having at the same time the minimum enhancement of kinetic energy in the rebound. Particles eventually crossing the surface are re-emitted with random Gaussian thermal velocities.

3.3.4 *Production and loss of particles*

Because SPH hates a void and requires at any time enough particles, it was assumed that the process of vapour emission could be activated by an impact, whose final result is a spherical plume of gas compressed and immediately over Ceres's surface, which expands under the effect of the pressure forces. This event can be an asteroidal or cometary impact, and the volatiles are released directly by the impacting object and/or by the region under the impact point, which, if rich in volatiles, can supply the H_2O vapour flux. So, different models can be developed, depending on whether a volatile H_2O source can be activated or not. If it can, it has different fluxes depending on the depth of the icy region. Here we have assumed the initial spherical plume to be composed of a mixture of H_2O vapour and dust, with the same mass ratio (3:1) as the material emitted by the surface. Anyway, a gas-free dusty plume could also be used. A plume dynamic model, without surface activation and emission, can be used as a reference zero-emission model (model B, see later).

The H_2O vapour can be lost by the central body directly (hydrodynamic loss). This happens when the molecules, accelerated up to sonic or supersonic velocities by the combined effect of pressure forces and thermal heating due to the Sun, maintaining some kind of collisional equilibrium, go beyond the Hill limit, and are conventionally considered lost. A single molecule can also escape by a different physical mechanism, when it is subjected to a sequence of collisions with the surrounding medium (other molecules plus dust particles plus thermal and solar photons up to its last collision), which allows it to reach the boundaries of the Hill lobe in a reasonable number of steps (we adopted an upper limit of 100). This is the characteristic thermal escape mechanism or Jeans escape (Hunten 1993). Then, at any time step of the dynamic SPH

Downloaded from https://academic.oup.com/mnras/article-abstract/455/2/1892/1108445 by guest on 07 May 2020

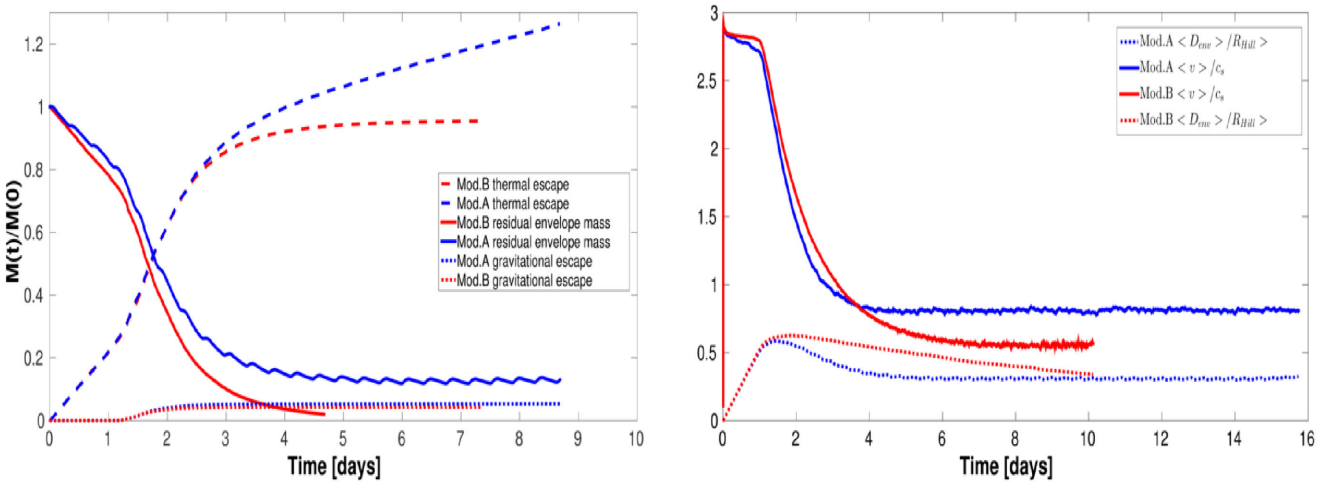

Figure 9. (a) Time evolution of the mass of the H_2O envelope for model A (blue line) with a surface emission of 6 kg s^{-1}, and model B (red line) with no emission. Masses are normalized to the initial H_2O mass. Dashed lines represent the fraction of mass lost by Jeans escape for model A (blue) and model B (red). Dotted lines show the fraction of mass lost by gravitational escape for model A (blue) and model B (red). The Jeans escape line overcomes the value 1, due to the surface H_2O emission. (b) Time evolution of the ratio of mean velocity of the H_2O vapour over sound velocity for model A (blue solid line) and model B (red solid line), and mean H_2O envelope radius over the Hill radius for model A (blue dashed line) and model B (red dashed lines). The mean velocity and envelope radius are computed in the barycentric reference frame of the envelope. The curves of model B stop when the H_2O mass drops under 10^{-3} of the initial mass. Here and in the other plots, the 9 h modulation is produced by the daily emission cycle.

evolution, a Monte Carlo sequence of virtual steps is produced for a sample molecule, one for each pseudo-particle. Each molecule having a number of virtual Monte Carlo steps less than the upper limit is added to an escape counter. By suitable procedures of normalization, this counter can produce a value of mass flux due to thermal escape. This mass flux comes, in principle, from all the pseudo-particles that deplete themselves up to the time of a possible complete disappearance.

At the same time, the surface region that is eventually activated emits gas and dust, which join the ensemble of particles and start to evolve with the same hierarchy as the other particles. The frequency of emission is controlled to respect the constraints on the gas/dust ratio and on the instantaneous emission from the cometary-like model.

Since the loss of particles can excessively reduce the resolution (space and time) of the SPH algorithm, a method has been developed to replenish each lost particle with a new one, obtained by splitting a random particle of the ensemble into two different components with a halved mass. The velocities and temperatures of the new particles are chosen to ensure momentum and energy conservation.

3.3.5 *Treatment of dust*

In principle, dust particles can be included, together with the gas molecules, in a SPH general treatment (Laibe & Price 2014a,b). Here, in the approximation of low values of the gas/dust ratio, we have followed the dynamic evolution of dust particles subjected to viscous drag with values of gas density, temperature and velocity vectors averaged over a suitable choice of pseudo-particles surrounding the selected dust particle. The choice was to include all the pseudo-particles inside a sphere of radius equal to the radius of influence (R_s) of the nearest pseudo-particle.

The conservation of total linear momentum can be ensured if the impulse gained (or lost) by a dust particle due to viscous forces is subtracted from (or added to) the pseudo-particles inside the sphere of interaction, using a random extraction criterion. Here we have utilized the viscous drag term, dependent on the Reynolds number, given by Weidenschilling (1977), which covers a satisfactory range of density and dust particle mass values. The viscous coupling timescale goes to zero together with the dust particle mass, and at the same time, it drives the integration time step. Low-mass dust particles produce an excessive growth of computing time. Then, we have assumed that particles with a coupling viscous timescale less than 0.2 times the local dynamic timescale, defined as $\tau_d = v_d/g_d$, v_d and g_d being the modules of velocity and acceleration of the particle, are completely coupled with the gas. They have velocities and accelerations equal to the mean gas values computed in the sphere of influence.

3.3.6 *SPH model results*

In Figs 9, 10 and 11 are plotted some significant parameters of the model of plume emission from Ceres, starting from a spherical cloud of H_2O vapour of 7.5×10^6 kg and 2.5×10^6 kg of dust, the latter having a power-law mass distribution $n(m) \propto m^{-1.2}$. The cloud is at Ceres's equator, at noon (local time) and having an altitude of 1.1 of its proper initial radius. The number of SPH particles is 3×10^4 for the vapour and 2×10^4 for the dust. We have developed two different models. Model A is characterized by post-impact activation, with a mean flux of H_2O (averaged over a complete Ceres rotation) of 6 kg s^{-1} and 10^{21} [SI]. In model B, the surface emission of H_2O and dust is not present.

From the figures it can be deduced that the initial expansion of the plume soon becomes strongly supersonic, with a balance of mass loss of 90 per cent of the initial vapour mass in about 3 d, well below the free thermal escape timescale $\tau_{th} = R_{Hill}/c_s$ of about 4.5 d. This is due to the strong hydrodynamic initial acceleration, which forces a large part of the vapour to reach the Hill boundary in a few days, and at the same time diluting the gas and producing very efficient mass loss by thermal escape. The thermal loss is present also in the initial expansion phase, and produces the moderate negative slope of the envelope mass plot (Fig. 9a, blue line). As soon as the front

Downloaded from https://academic.oup.com/mnras/article-abstract/455/2/1892/1108445 by guest on 07 May 2020

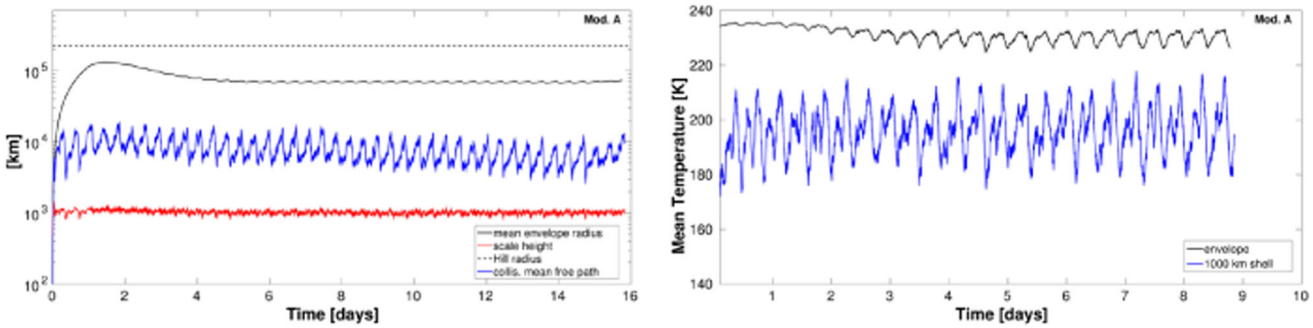

Figure 10. (a) Vertical scale height (red solid line) and collisional mean free path of H_2O (blue solid line), compared with the mean envelope radius (black solid line) and with the Hill radius (black dashed line). The scale height and mean free path are computed in a spherical shell 1000 km thick over Ceres's surface. (b) Mean temperature of the 1000-km shell (blue) and mean envelope temperature (black). Both figures are for model A.

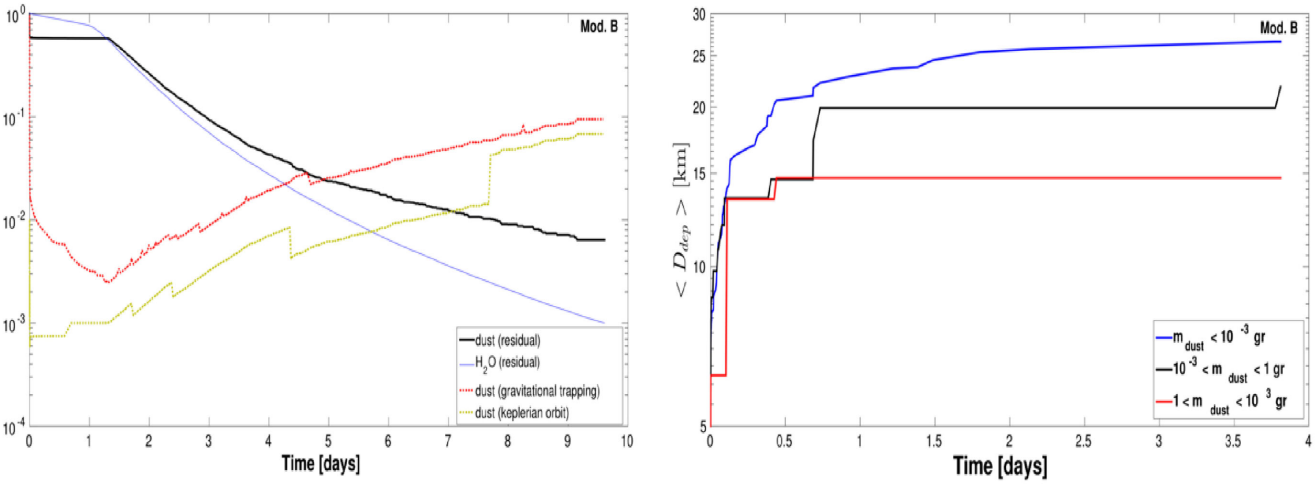

Figure 11. (a) Comparison of the relative masses of H_2O (blue solid line) and dust (black solid line), referred to their initial masses. The fraction of the dust mass gravitationally trapped inside the Hill lobe (red dotted line) and the dust mass fraction in a Keplerian elliptical orbit, with pericentre over Ceres's surface (green dotted line), are shown. These two last masses are referred to as the running value of the dust mass, $M_d(t)$. The abrupt decrease of the dust mass is due to the initial steep deposition of solid particles on the surface. (b) Mean value of the distance of the dust deposited on Ceres's surface, for three classes of dust mass. The distance is computed from the projection on Ceres's surface of the initial centre of the plume. The jumps in both figures are due to the finite number of dust particles and to the discontinuous selection criteria for the different properties of the particles. Both figures are for model B.

of the expanding envelope reaches the boundary of the Hill lobe, there is a direct loss of matter due to the crossing of the Hill boundary itself, and at the same time the mass loss timescale becomes smaller (about 4 d) due to the dilution of the gas and the increased efficiency of the thermal escape process. The region beyond about half of the Hill radius is then strongly depleted (Fig. 9b). When the majority of the initial plume is lost, a residual of gas remains with a nearly sonic mean velocity, confined within a few Ceres radii. It is more subject to the day–night cycle, with lower mean temperatures and evaporating with a timescale of about 15–20 d. This is the scenario when there is no surface activation. If the impact (or any possible trigger mechanism) causes vapour emission from the surface as described before, there can be a significant accumulation of gas near the surface. The molecules emitted find a medium with a low collisional mean free path, low pressures and a periodic nightly temperature drop, with possible alternating condensation and sublimation. A fraction of about 15 per cent of the initial mass of the plume is present around Ceres, modulated in time together with the modulation of the vapour emission. This modulation is present also in the physical parameters of the near surface region (Figs 9 and 10). This gas layer has a depth of few Ceres radii.

Figs 10(a) and (b) show the mean values, averaged over a spherical shell extending 1000 km over Ceres's surface, of the gas scale height, the collisional mean free path and the temperature. The choice of 1000 km for the extension of the averaging shell for density and other physical quantities, comparable with the gas scale height itself, makes the computation self-consistent. In the plots, mean values of the envelope radius and temperature are also represented. The scale height is defined as $H_{sh} = (M_{shell}/(4/3\pi\,\rho_{shell}))^{1/3}$. M_{shell} is the mass inside the shell and ρ_{shell} is the mean density inside the shell.

Some preliminary results on the combined evolution of a mixture of dust and water vapour are plotted in Figs 11(a) and (b). The dust does not experience thermal escape, so three possibilities are present from short to long timescales: acceleration beyond the Hill limit, deposition on Ceres's surface and Keplerian orbits around the planet. Although the results are deeply dependent on the initial assumptions for the dust (and gas) parameters, a non-negligible fraction of the dust initially contained in the plume or emitted by the active surface can be inserted in nearly stable orbits (Fig. 11a). The stability strongly depends on the orbital parameters. After 10 d, a fraction of about 10^{-3} remains in Keplerian orbits, while 25 per cent

Downloaded from https://academic.oup.com/mnras/article-abstract/455/2/1892/1108445 by guest on 07 May 2020

has been redeposited and 70 per cent was expelled due to gas acceleration. The remaining 5 per cent is merged in the gas envelope. The surface deposition clearly depends on the mass of the dust particles. Those with smaller masses are well mixed by the gas and show longer redeposition timescales. For all the particles, the mean deposition radius is a few tens of kilometres (Fig. 11b), i.e., the typical ballistic range of a velocity field centred on the sound velocity.

4 DISCUSSION AND CONCLUSIONS

Herschel observations of water emission (Küppers et al. 2014) suggest a flux of at least 10^{26} mol s^{-1} (or, analogously 6 kg s^{-1}). Küppers et al. (2014), by applying a thermo-physical model, estimated the emitting area (0.6 km^2). Our simulations suggest that ice exposed on the surface is very unstable, so it is difficult to explain such emission due to fresh ice concentrated in an area of less than 1 km^2. Only for a very short period, less than 10 yr (as also suggested by Titus 2015), is the water flux value around 10^{20} [SI], so an emitting area of less than 1 km^2 is plausible. After this transient phase, the water ice sublimation front is buried under a dusty crust and the water flux decreases to 10^{18} [SI], remaining stable for a very long time. In this case, an emitting area of 100 km^2 is necessary to match the Herschel observations. If the ice is very far below the surface (i.e., 100 m), an emitting area of 10^7 km^2 is required, which is greater than the overall area of Ceres, thus this is impossible. In all the scenarios we developed, the ice is not stable for a long time on the surface at mid and equatorial latitudes. At high latitudes, the water flux is so small that it cannot fit the observed values.

From these scenarios, it is clear that the only way to have sufficient water flux to match the Herschel observations is to have the ice not very far from the surface (a depth of a few centimetres, compatible with the annual skin depth).

Alternatively, a continuous replenishment of fresh ice is required. A possible mechanism could be impacts with other bodies, which could remove the blanket of dust. However, the rate of impacts is not compatible with the life of the exposed ice on the surface. For this purpose, an area of 1 km^2 is expected to be activated every 1400–7700 yr, with an excavated depth of about 200–250 m (the uncertainty depends on the physical properties of the terrain). The activation rate is calculated from impact cratering (the frequency of formation of a crater of at least 1 km in diameter is 4.5×10^{-11} to 2.5×10^{-10} km^{-2} yr^{-1}) (S. Marchi, personal communication).

Since Ceres is a transition object between the outer and the inner Solar system, it seems to require an ad hoc mechanism to explain its water emission. Observation data so far available do not allow us to discriminate among the possible mechanisms, even if the revealed water emission seems to exhibit a variability with the heliocentric distance. Here we propose that, to match the values obtained by Herschel (Küppers et al. 2014), sublimation from subsurface ice layers (very close to the surface and with a large emitting area) is a plausible emission mechanism. Support for this mechanism could be subsurface convection due to some kind of internal energy source and/or long-term activation of regions that have experienced previous impacts. To find eventual markers of past (or present) more or less extended regions of H_2O emission, it would be interesting to study the post-impact phases on short timescales, focusing on the behaviour of the dust and on the dynamic effect of the gas.

For this reason, numerical simulations of the evolution of a plume generated by an impact, or by some kind of abrupt discontinuity of the surface that ultimately releases H_2O ice, can help us to understand if these phenomena, whose frequency is still unknown, could have left observable signatures on Ceres's surface. The free evolution timescale of the gaseous plume is of the same order of magnitude, and not much larger than, the Jeans thermal loss timescale, i.e., from a few to several days. Nevertheless, it has been shown that a nearly isothermal optically thin envelope can form in association with the emission of H_2O from the surface. The envelope follows the evolution of the emission process from the surface, and vanishes together with the H_2O emission. The structure of the envelope, with a 6 kg s^{-1} flux, is on the borderline between an exosphere and a true atmosphere. Its main influence on the pseudo-cometary emission is probably through the dust deposition process of the dust decoupled from the gas. The more massive impacts that in the past produced the largest craters observed on Ceres are different. They could require a mass of H_2O vapour several (3–8?) orders of magnitude greater than that responsible for the Herschel observations, and a true LTE transient envelope possibly should have been formed. Significant fractions of the dust released could have been redeposited and left in long-time stable bound orbits around the planet.

In summary, the likely scenarios useful to explain the water vapour emission could be:

(i) cometary-type sublimation
(ii) cryo-volcanism
(iii) transport from the interior (subsurface convection)
(iv) impacts

While cryo-volcanism and transport from the interior could not be tested with our simulations, cometary-type sublimation (from subsurface layers) is proposed as a feasible mechanism. Moreover, impacts could activate the surface and expose fresh ice from the interior.

Even if Ceres seems to be homogeneous on a large scale, the missions *Herschel* (Küppers et al. 2014) and more recently *Dawn* have discovered single structures with a high albedo. In particular, *Dawn* has shown that these bright spots are largely diffused. According to our results, they are not exposed ice spots. However, some of them could be linked to the emission of water (present? past?). The dust distribution on Ceres's surface could provide answers for how water emission is linked to the bright spots.

Finally, the *Dawn* mission will soon give new insights about the possible mechanisms responsible for water emission and the presence of exposed ice on the surface.

ACKNOWLEDGEMENTS

We want to thank Dr M. Kueppers for useful suggestions and comments. This work is supported by an Agenzia Spaziale Italiana (ASI) grant. The computational resources used in this research were supplied by Istituto Nazionale di Astrofisica (INAF-IAPS) through the DataWell project.

REFERENCES

A'Hearn M. F., Feldman P. D., 1992, Icarus, 98, 54
Capria M. T., Marchi S., de Sanctis M. C., Coradini A., Ammannito E., 2012, A&A, 537, A71
Carry B., Dumas C., Fulchignoni M., Merline W. J., Berthier J., Hestroffer D., Fusco T., Tamblyn P., 2008, A&A, 478, 235
Castillo-Rogez J. C., McCord T. B., 2010, Icarus, 205, 443
Chamberlain M. A., Sykes M. V., Esquerdo G. A., 2007, Icarus, 188, 451
Chamberlain M. A., Lovell A. J., Sykes M. V., 2009, Icarus, 202, 487
De Sanctis M. C., Lasue J., Capria M. T., Magni G., Turrini D., Coradini A., 2010a, Icarus, 207, 341
De Sanctis M. C., Lasue J., Capria M. T., 2010b, AJ, 140, 1

Downloaded from https://academic.oup.com/mnras/article-abstract/455/2/1892/1108445 by guest on 07 May 2020

Fanale F. P., Salvail J. R., 1989, Icarus, 82, 97
Hunten D. M., 1973, J. Atmos. Sci., 30, 1481
Hunten D. M., 1993, Science, 259, 915
Keihm S., Kamp L., Gulkis S., Hofstadter M., Lee S., Janssen M., Choukroun M., 2013, Icarus, 226, 1086
Klinger J., 1980, Science, 209, 271
Krause M., Blum J., Skorov Y. V., Trieloff M., 2011, Icarus, 214, 286
Küppers M. et al., 2014, Nature, 505, 525
Laibe G., Price D. J., 2014a, MNRAS, 440, 2136
Laibe G., Price D. J., 2014b, MNRAS, 440, 2147
Lasue J., De Sanctis M. C., Coradini A., Magni G., Capria M. T., Turrini D., Levasseur-Regourd A. C., 2008, Planet. Space Sci., 56, 1977
Liu M., Liu G., 2010, Archives Comput. Methods Eng., 17, 25
Magni G., 2014, European Planet. Sci. Congress 2014, EPSC Abstracts, Vol. 9, EPSC2014-599, p. 599
Magni G., Coradini A., 2004, Planet. Space Sci., 52, 343
McCord T. B., Sotin C., 2005, J. Geophys. Res. (Planets), 110, 5009
McCord T. B., Castillo-Rogez J., Rivkin A., 2011, Space Sci. Rev., 163, 63
Monaghan J. J., 1992, ARA&A, 30, 543
Monaghan J., 1994, J. Comput. Phys., 110, 399
Monaghan J. J., 2005, Rep. Progress Phys., 68, 1703
Russell C. T., Raymond C. A., 2011, Space Sci. Rev., 163, 3
Saint-Pe O., Combes M., Rigaut F., 1993, Icarus, 105, 271
Shoji D., Kurita K., 2014, J. Geophys. Res. (Planets), 119, 2457
Spencer J. R., 1990, Icarus, 83, 27
Thomas P. C., Parker J. W., McFadden L. A., Russell C. T., Stern S. A., Sykes M. V., Young E. F., 2005, Nature, 437, 224
Titus T. N., 2015, J. Geophys. Res. (Planets), 42, 2130
Tosi F. et al., 2015, in Lunar and Planetary Inst. Technical Report, Vol. 46, Lunar and Planetary Science Conference, p. 1745
Tu L., Ip W.-H., Wang Y.-C., 2014, Planet. Space Sci., 104, 157
Weidenschilling S. J., 1977, MNRAS, 180, 57

This paper has been typeset from a TEX/LATEX file prepared by the author.

Downloaded from https://academic.oup.com/mnras/article-abstract/455/2/1892/1108445 by guest on 07 May 2020